Journal of
Materials Chemistry A

REVIEW

Cite this: *J. Mater. Chem. A*, 2019, **7**, 3531

Recent progress in electrocatalytic nitrogen reduction

Xiaoxi Guo,[a] Huitong Du,[a] Fengli Qu *[a] and Jinghong Li [b]

Ammonia (NH_3) is an activated nitrogen building block for the manufacture of modern fertilizers, plastics, fibers, explosives, *etc.*; however, its production is limited to the traditional Haber–Bosch process. Very recently, electrocatalytic reduction of nitrogen (N_2) has been demonstrated to be a clean and sustainable approach to produce NH_3, which has aroused widespread attention. All types of electrocatalysts have been developed and designed for the electrochemical nitrogen reduction reaction (NRR). To achieve both high catalytic performance and selectivity, electrocatalysts must be rationally designed to optimize the mass transport, chemi(physi)sorption, and transfer of protons and electrons. In this review, we summarize the recent developments on electrocatalysts for N_2 fixation. First, we discuss the reaction mechanisms of the NRR. Second, three categories of electrocatalysts according to their chemical compositions are surveyed. Then, the effects of different types of electrolytes on NRR activity and electrolyte choice are also summarized. Finally, the existing challenges and future perspectives are discussed.

Received 21st November 2018
Accepted 28th January 2019

DOI: 10.1039/c8ta11201k

rsc.li/materials-a

1. Introduction

With the pressing energy crisis, growing environmental concerns and increasing global population, it is urgent to search for sustainable, green and economic strategies to solve tricky problems.[1,2] The development of efficient electrocatalysts is regarded as an energy-saving and eco-friendly approach, which can be used to produce fuels and value-added chemicals, including hydrogen (H_2), oxygenates, hydrocarbons and ammonia (NH_3) from earth-abundant feedstock such as water, oxygen, carbon dioxide and nitrogen (N_2). In the past few years, considerable efforts have been devoted to developing and designing numerous electrocatalysts toward the hydrogen evolution reaction (HER),[3–5] oxygen evolution reaction (OER),[6–8] oxygen reaction reduction (ORR)[9–11] and carbon dioxide reduction reaction (CO_2RR).[12–14] However, electrochemical reduction to form NH_3 from N_2 and H_2O has not been fully explored yet, although artificial N_2 fixation has been investigated for more than 100 years.[15,16]

NH_3, as a green energy carrier, potential transportation fuel and chemical for fertilizer synthesis, plays an indispensable role in the agricultural, plastic, pharmaceutical and textile industries.[17–19] Thus far, there are three typical pathways to

Xiaoxi Guo received her Bachelor's degree from Qufu Normal University in 2017. She is now pursuing her Master's degree at the College of Chemistry and Chemical Engineering at Qufu Normal University. Her current research interests mainly focus on electrochemical water splitting and photoelectrochemistry.

Huitong Du received his Bachelor's degree from Qufu Normal University in 2016. He is currently a Master's student at Qufu Normal University. His current research interests include developing electrocatalysts for water splitting and electrochemical nitrogen reduction reaction.

---

[a] College of Chemistry and Chemical Engineering, Qufu Normal University, Qufu 273165, Shandong, China. E-mail: fengliquhn@hotmail.com

[b] Department of Chemistry, Key Laboratory of Bioorganic Phosphorus Chemistry & Chemical Biology, Tsinghua University, Beijing 100084, China

synthesize NH_3: azotobacter nitrogen fixation, Haber–Bosch process and electrocatalysis (Scheme 1). In nature, biological N_2 fixation is performed under mild conditions *via* nitrogenase enzymes. Although this method can achieve maximum electron efficiency and low energy efficiency, its practical applications are restricted by its ultralow reaction rate.[20] Currently, industrial NH_3 synthesis still heavily relies on the conventional Haber–Bosch process using heterogeneous iron- or ruthenium-based catalysts at high temperature (300–500 °C) and high pressure (150–300 atm), which accounts for over 1% total global fossil energy and causes more than 300 million metric tons of CO_2 emissions annually.[21,22] Accordingly, it is highly desirable to develop eco-friendly and sustainable strategies to replace the energy-consuming and environment-polluting Haber–Bosch process. The electrochemical reduction process using heterogeneous catalysts has great potential to achieve clean, carbon-free and sustainable NH_3 production from N_2 and H_2O directly since it can be performed under ambient conditions employing renewable solar and wind energy.[23–26] Most importantly, in the renewable-electricity-driven electrochemical N_2 reduction reaction (NRR) system, electrocatalysts are the paramount components. Thus, it is a priority to rationally design and synthesize NRR electrocatalysts.

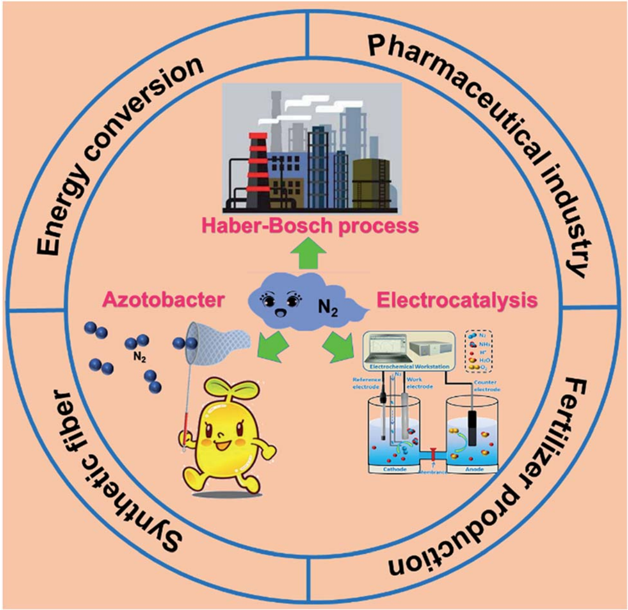

Scheme 1 Three typical pathways of nitrogen fixation and their applications.

To date, a series of electrocatalysts have been developed and constructed to produce NH_3. These catalysts can be mainly classified to three types: noble metal-based electrocatalysts, non-noble metal-based electrocatalysts and metal-free electrocatalysts. It is generally acknowledged that the morphology (size, shape, dimension, *etc.*), crystallinity, density of surface active sites, intrinsic electronic structure, *etc.* highly affect the activity of catalysts. Hence, the properties of NRR electrocatalysts can be boosted by generating porous structures, and increasing the surface area of materials along with constructing two- or three-dimensional nanostructures to expose their active sites adequately. Furthermore, heteroatom doping and defect engineering with amorphism can tune the intrinsic electron structure of catalysts to obtain high catalytic activity. During the process of electroreduction, the main side reaction is the HER,[27,28] in which most protons or H_2O in the system are reduced to H_2 rather than NH_3,[29,30] causing a severe selectivity issues. The involved equations with the equilibrium potentials referenced to the reversible hydrogen electrode (RHE) and standard hydrogen electrode (SHE) are as follows:

$$N_2 + 6H^+ + 6e^- \leftrightarrow 2NH_3(g),\ E^0 = 0.148\ \text{V}\ vs.\ \text{RHE} \quad (1)$$

$$2H^+ + 2e^- \leftrightarrow H_2,\ E^0 = 0\ \text{V}\ vs.\ \text{SHE at pH} = 0 \quad (2)$$

$$N_2 + 6H_2O + 6e^- \leftrightarrow 2NH_3 + 6OH^-,\ E^0 = -0.763\ \text{V}\ vs.\ \text{SHE at pH} = 14 \quad (3)$$

$$2H_2O(l) + 2e^- \leftrightarrow H_2(g) + 2OH^-,\ E^0 = -0.828\ \text{V}\ vs.\ \text{SHE at pH} = 14 \quad (4)$$

Fengli Qu received her Ph.D. degree in Analytical Chemistry in Hunan University (China) in 2008. She worked in LCPME-CNRS (Nancy, France) as a Postdoctoral Fellow from 2008 to 2009 and as a Visiting Professor in Princeton University (Princeton, USA) from 2013 to 2014. Currently, she is a Professor in the College of Chemistry and Chemical Engineering at Qufu Normal University. Her research interests include nanomaterial applications and biosensor development.

Jinghong Li is currently a Cheung Kong Professor at the Department of Chemistry at Tsinghua University, China. He received his PhD degree from Changchun Institute of Applied Chemistry, Chinese Academy of Sciences in 1996. He joined the Faculty of Tsinghua University in 2004. His current research interests include electroanalytical chemistry, bioelectrochemistry and sensors, physical electrochemistry and interfacial electrochemistry, electrochemical materials science and nanoscopic electrochemistry.

It can be seen from the chemical equations that the equilibrium potentials of NRR and HER ((1) *vs.* (2) and (3) *vs.* (4)) are similar in both acidic and alkaline electrolytes, which indicates that HER is the major competing reaction. Thus, selectivity for the NRR should be considered. Active composition, crystal structure, surface properties that prefer strong binding with N-adatoms to H-adatoms, and good electrical conductivity are conducive to suppress the HER and enhance efficiency. In addition, as an indispensable reaction medium during electrochemical processes, the electrolyte can also greatly affect the NRR activity and selectivity. An electrolyte with a limited proton transfer rate and increases the solubility of N_2 can efficiently improve the selectivity. Hence, it is highly necessary to choose and develop ideal electrolytes for a specific electrolytic NRR cell. Additionally, catalysts suffer from deactivation and decomposition in the electrocatalytic process, which limit their practical applications. Therefore, stability should be taken into account when designing and developing electrocatalysts.

In this review, we summarize the recent development on electrocatalysts for N_2 fixation. First, we discuss the reaction mechanisms of the NRR. Second, three categories of electrocatalysts according to chemical compositions are surveyed. Then, the effects of different types of electrolytes (liquid electrolytes, polymer electrolytes, molten salt electrolytes and solid oxide electrolytes) on the NRR activity and electrolyte choice are also presented. Finally, the existing challenges and future perspectives are discussed.

2. Reaction mechanisms of NRR

Electrochemical NRR involves a multistep proton-electron transfer process and multiple intermediates, represented as follows:[31,32]

$$N_2 + H^+ + e^- \leftrightarrow N_2H,\ E^0 = -3.2\ \text{V}\ \textit{vs.}\ \text{RHE} \tag{5}$$

$$N_2 + 2H^+ + 2e^- \leftrightarrow N_2H_2(g),\ E^0 = -1.10\ \text{V}\ \textit{vs.}\ \text{RHE} \tag{6}$$

$$N_2 + 4H^+ + 4e^- \leftrightarrow N_2H_4(g),\ E^0 = -0.36\ \text{V}\ \textit{vs.}\ \text{RHE} \tag{7}$$

$$N_2 + 4H_2O + 6e^- \leftrightarrow N_2H_4 + 4OH^-,\ E^0 = +0.55\ \text{V}\ \textit{vs.}\ \text{RHE at pH} = 14 \tag{8}$$

$$N_2 + e^- \leftrightarrow N_2^-(aq),\ E^0 = -3.37\ \text{V}\ \textit{vs.}\ \text{RHE at pH} = 14 \tag{9}$$

As shown, the redox potentials of reactions (5) and (6) are much more negative compared to that of reaction (2), which indicates that it is difficult to form N_2H and N_2H_2 intermediates and easy to conduct H^+ reduction. In a strong alkaline electrolyte, reaction (9) will compete with reaction (5). On the contrary, the second and third bonds of the N_2 molecule are very weak, resulting in lower redox potentials for the four-electron (reaction (7)) and six-electron reduction (reaction (8)) processes than the first-electron and two-electron reduction processes. Because of the multistep proton–electron transfer process and multiple intermediates of the NRR, its reaction mechanisms have not been elaborated completely. Typically, the reaction mechanisms of the NRR can be divided into two types: associative and dissociative mechanisms (Fig. 1a).[33] During the associative mechanism, the N_2 molecule is adsorbed on the catalyst surface and then, the hydrogenation process proceeds. In addition, the hydrogenation process involves two approaches: distal and alternating pathways. In the distal pathway, hydrogenation preferentially occurs on the N atom far away from the surface of catalyst. When the first NH_3 molecule is formed and released, the N atom bound to the surface of the catalyst begins hydrogenation and produces a second NH_3 molecule, while the hydrogenation alternates between two N molecules in the alternating processes. After the first NH_3 molecule is released, the second one is released closely. Moreover, the dissociative pathway is applied for industrial production processes. In the dissociative mechanism, the N≡N triple bond is broken first and then, the two N atoms adsorbed on the catalyst surface undergo a hybrid process independently.

In 2009, theoretical calculations of the possibility of producing NH_3 electrochemically at ambient conditions were studied by Nørskov and co-workers.[34] They calculated the free energy profile for the reduction of N_2 admolecules and N adatoms on several close-packed and stepped transition metal surfaces in an acidic electrolyte, revealing the relationship between the adsorption of N species on the electrocatalyst surface and catalytic performance for NH_3 formation. Fig. 1b shows a volcano diagram for flat (black) and stepped (red) transition metal surfaces for the reduction of N_2 with a Heyrovsky-type reaction, including dissociative (solid lines) and associative (dashed lines) mechanisms, without (solid lines) and with (dotted lines) H-bonds. As observed, the most active surfaces, which are at the top of the volcano diagrams, are Mo, Fe, Rh, and Ru, but these surfaces are predicted to be more active for promoting the HER rather than the NRR, which will render a low FE. At the right leg of the volcano diagram, Rh, Ru, Ir, Co, Ni, and Pt prefer to absorb H-adatoms for the HER. Since the flat metal surfaces of early transition metals such as Sc, Y, Ti, and Zr bind N-adatoms more strongly than H-adatoms, significantly higher production of NH_3 compared with that of H_2 can be expected on these metal electrodes at the theoretical applied bias of ≈ −1.0 to −1.5 V. However, these metal surfaces are easily oxidized, thus it hard to predict whether they are efficient NRR electrocatalysts or not.

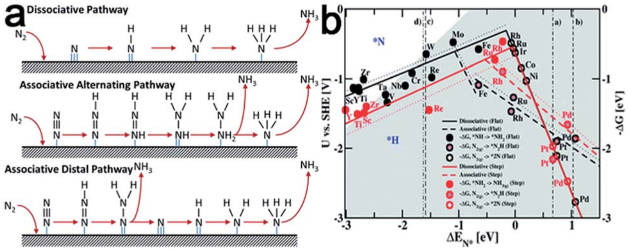

Fig. 1 (a) Possible reaction mechanisms for the NRR to form NH_3. Reproduced with permission from ref. 33 copyright 2017, Elsevier. (b) Dissociative (solid lines) and associative (dashed lines) mechanisms, without (solid lines) and with (dotted lines) H-bonds effect on both flat (black) and stepped (red) metal surfaces. Reproduced with permission from ref. 34. Copyright 2012, RSC.

3. Electrocatalysts for the NRR

Recently, significant efforts have been devoted to designing and fabricating NRR electrocatalysts. To sum up, three categories of electrocatalysts according to their chemical compositions have been reported, including noble metal electrocatalysts, non-noble metal electrocatalysts and metal-free electrocatalysts. In this section, we elaborate on the NRR performance of these electrocatalysts.

3.1 Noble metal-based electrocatalysts for the NRR

Noble metals have marvelous conductivity, possess active polycrystalline surfaces and bind with a wide range reactants; thus, they are competent as efficient electrocatalysts for numerous reactions. Intriguingly, precious metals have been reported as appealing electrocatalysts for the NRR. Recently, noble-metals-based catalysts such as Au,[35–39] Ru,[41,42] Pt,[43,44] and Rh[45] have been widely investigated. The activity of noble metal-based electrocatalysts is displayed in Table 1.

Typical research on NRR electrocatalysts containing Au was conducted by Yan's group. In their study, they synthesized tetrahexahedral gold nanorods (THH Au NRs) *via* a seeded growth method using a binary surfactant mixture.[37] The as-synthesized THH Au NRs were enclosed by a stepped {730} facet composed of (210) and (310) sub-facets and exhibited comparable NRR activity (NH_3: 1.648 μg h^{-1} cm^{-2} and $N_2H_4 \cdot H_2O$: 0.102 μg h^{-1} cm^{-2}) at −0.2 V *vs.* RHE in 0.1 M KOH. However, their NH_3 yield and faradaic efficiency (FE) were too low for practical applications. It is likely that the surfactant molecules used in the synthesis process remained on the surface of the THH Au NRs and covered the active sites of the catalyst, resulting in a relatively low NH_3 production rate. Accordingly, removal of the surfactant molecules and constructing two- or three-dimensional nanostructures may increase the density of active sites. Recently, Nazemi *et al.* fabricated hollow gold nanocages (AuHNCs) (Fig. 2a and b) from a silver solid nanocube (AgNC) template the galvanic replacement technique without surfactant.[38] The NRR electrocatalytic performance of the AuHNCs was comparable to that of solid Au nanoparticles of various shapes such as rods, spheres and cubes, which is mostly due to the increased surface area and confinement of the reactants in their cavity (cage effect). As shown in Fig. 2c, the NRR activity was tested in a double-chamber H-type cell, which was filled with 0.5 M $LiClO_4$ aqueous solution as the electrolyte. As shown in Fig. 2d, the highest FE (30.2%) was achieved at −0.4 V *vs.* RHE, while the highest NH_3 yield rate (3.9 μg h^{-1} cm^{-2}) was obtained at −0.5 V *vs.* RHE.

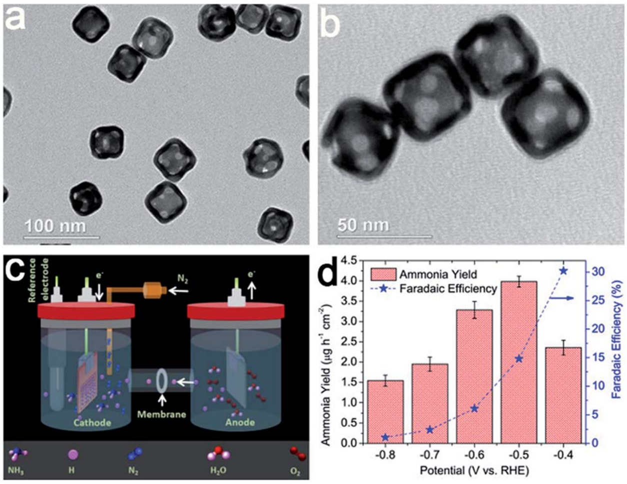

Fig. 2 (a) and (b) TEM images of AuHNCs with different magnifications. (c) Schematic of an electrochemical cell for the NRR. (d) NH_3 yield rate and FE at various potentials in 0.5 M $LiClO_4$ at 20 °C. Reproduced with permission from ref. 38, copyright 2018, Elsevier.

Ru shows high activity because it can satisfy the activation energy barrier, surface vacant sites, and the number of step sites. Dahl *et al.* used DFT to investigate the stepped surface of Ru, which was beneficial for low-barrier N_2 dissociation and a more reactive NH_3 synthesis process than that provided by the Au-passivated Ru surface.[40] Kordali and co-workers developed Ru/C for NH_3 production with the rate of NH_3 synthesis of 0.21 μg h^{-1} cm^{-2} at −1.10 V *vs.* Ag/AgCl.[41] However, Ru catalysts are prone to hydrogen adsorption (hydrogen poisoning), a problem that results in NRR inhibition. Manjunatha *et al.* prepared a ruthenium–platinum alloy (1 : 1) dispersed on a Vulcan XC-72 carbon composite (RuPt/C), which showed a comparable performance (18.36 μg h^{-1} cm^{-2} with 13.2% FE at an applied potential of 0.123 V *vs.* RHE) for the metallic ruthenium and

Table 1 Summary of the representative reports on N_2 electroreduction and NH_3 formation using noble metal catalysts

Catalyst	Electrolyte	Temperature	NH_3 Yield	FE (%)	Potential	Ref.
TA[a]-reduced Au/TiO_2	0.1 M HCl	20 °C	21.4 μg h^{-1} cm^{-2}	8.11	−0.2 V *vs.* RHE	35
a-Au/CeO_x–RGO	0.1 M HCl	25 °C	1.66 μg h^{-1} cm^{-2}	10.10	−0.2 V *vs.* RHE	36
THH Au NRs	0.1 M KOH	25 °C	1.648 μg h^{-1} cm^{-2}	4.02	−0.2 V *vs.* RHE	37
AuHNCs	0.5 M $LiClO_4$	20 °C	3.9 μg h^{-1} cm^{-2}	30.2	−0.4 V *vs.* RHE	38
Au flowers	0.1 M HCl	Room temperature	10.23 μg h^{-1} cm^{-2}	6.05	−0.2 V *vs.* RHE	39
Ru/C	2.0 M KOH	20 °C	0.21 μg h^{-1} cm^{-2}	0.28	−1.1 V *vs.* Ag/AgCl	41
RuPt/C	1.0 M KOH	50 °C	18.36 μg h^{-1} cm^{-2}	13.2	1.23 V *vs.* RHE	42
Pt/C	0.5 M H_2SO_4	Room temperature	69.8 μg h^{-1} cm^{-2}	0.5	1.6 cell voltage	43
Pt/C	$Li^+/H^+/NH_4^+$ electrolyte	80 °C	47.2 μg h^{-1} cm^{-2}	0.83	1.2 cell voltage	44
Rh NNs	0.1 M KOH	Room temperature	7.45 mg h^{-1} cm^{-2}	0.217	−0.2 V *vs.* RHE	45

[a] TA: tannic acid.

platinum catalysts.[42] In their study, they claimed that RuPt displayed a synergistic effect toward the electrochemical formation of ammonia due to co-catalysis. At the dual RuPt surface site, N_2 adsorbed on an Ru site reacts with the H_2 anchored on a Pt site in the NH_3 evolution reaction.

Lan *et al.* employed platinum supported on carbon black (Pt/C) catalyst as both the cathode and anode electrodes for NH_3 production directly from air and water at ambient conditions.[43] Using air and water as the feedstock is a renewable and sustainable chemical synthesis process for the future. The NH_3 production rate of the as-obtained Pt electrocatalyst (loading: 1 mg cm^{-2}) was 69.8 μg h^{-1} cm^{-2} at a current efficiency of ∼0.5 at 1.6 V. However, its extremely low FE is far from satisfactory. Later, they introduced an $H^+/Li^+/NH_4^+$ mixed conducting Nafion membrane into the electrocatalytic system.[44] The Li^+ ions hinder proton transfer and render a lower current at a higher applied voltage. Additionally, the mass loading of Pt catalysts should be reduced to lower their cost and decrease the HER competition. Moreover, Pt is not a good anodic reaction electrocatalyst, and its large overpotential is adverse for NH_3 formation. Notably, the NH_4^+ ion mixed in the Nafion membrane may affect the accurate determination of NH_3.

Very recently, Rh-based materials have been reported to be good NRR electrocatalysts. Chen's group fabricated surfactant-free atomically ultrathin Rh nanosheet nanoassemblies (Rh NNs) (Fig. 3a) using a cyanogel-reduction method.[45] Almost all precious metal nanosheets are synthesized in the presence of surface-capping agents, which cover the active sites and hinder the surface reaction, and thus result in an unfavorable effect on the electrocatalytic activity. In their study, the Rh NNs were synthesized from an inorganic polymer $RhCl_3$–$K_3Co(CN)_6$ cyanogel. The resulting catalyst possessed an ultrathin nanosheet structure with the thickness of 1.0–1.1 nm (Fig. 3b). As shown in Fig. 3c, the surfactant-free Rh NNs exhibited a high NH_3 yield of 7.45 mg h^{-1} cm^{-2} with no N_2H_4 detected at a low potential (−0.2 V *vs.* RHE) in 0.1 M KOH. Fig. 3d demonstrates the Rh NNs suffered from a severe competing HER, which rendered a low FE. Additionally, it remains unknown whether CN^- leads to NH_3 contamination during electrocatalytic measurements.

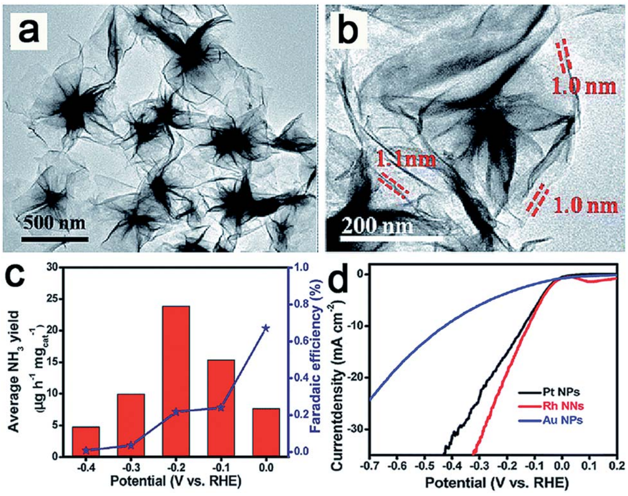

Fig. 3 (a) TEM and (b) HRTEM images of Rh NNs. (c) NH_3 yield rate and FE in N_2-saturated 0.1 M KOH electrolyte at different applied potentials. (d) LSV curves of Rh NNs (red), Au nanoparticles (blue) and Pt nanoparticles (black) for the HER in Ar-saturated 0.1 M KOH electrolyte at 50 mV s^{-1}. Reproduced with permission from ref. 45. Copyright 2018, RSC.

3.2 Non-noble metal-based electrocatalysts for the NRR

Non-noble metal-based NRR materials, particularly transition-metal-based NRR materials, have been widely studied as NRR electrocatalysts (Table 2) due to their low cost, earth-abundant reserves, and availability of d-orbital electrons for π-back donation, which can alleviate kinetic issues for N_2 activation.[50,70] In nature, biological N_2 fixation occurs under mild conditions *via* nitrogenase enzymes that contain non-noble-metal cofactors as catalytic active sites such as FeMo, FeV, and FeFe.[46,47] Therefore, the development of nonprecious metal catalysts to stimulate the nitrogenase catalytic process has great prospects. In the following part, we will discuss the recently reported NRR electrocatalysts based on non-noble metals.

Inspired by natural enzymes, Mo-based electrocatalysts have been intensively investigated.[48–51] Sun's group reported an MoS_2 nanosheet array grown on carbon cloth (MoS_2/CC) as an active material for the NRR, achieving an FE of 1.17% and NH_3 yield of 4.94 μg h^{-1} cm^{-2} at −0.5 V *vs.* RHE in 0.1 M Na_2SO_4.[48] In addition, the calculated isosurface of deformation charge density indicated that the positive charge mainly locates around the Mo atoms, which plays a key role in polarizing and activating N_2 molecules. In the NH_3 synthesis process, the charge transferred from N_2 to the positively charged Mo-edge, resulting in the formation of an N–Mo bond and the notable weakening of the N≡N triple bond. The DFT calculations also demonstrated that the edge of MoS_2 appears to be an electrocatalytically active site toward the HER; thus, this catalyst cannot suppress the competing reaction well. Later, Cheng *et al.* synthesized molybdenum carbide nanodots embedded in ultrathin carbon nanosheets (Mo_2C/C) to somewhat reduce the HER.[50] Form the aspect of the d orbital theory, Mo_2C, a transition metal carbide with unoccupied d orbitals, exhibits highly efficient adsorption behaviour for electron-enriched substances, such as N_2.[52,70] As shown in Fig. 4a, Mo_2C/C was constructed *via* the molten salt synthesis method. The SEM image showed that the as-synthesized Mo_2C/C sample had an evident nanosheet structure characteristic (Fig. 4b). In Fig. 4c, the high-resolution TEM (HRTEM) image shows ultra-small nanoparticles a the size of 2–3 nm uniformly embedded on the carbon nanosheet. The as-synthesized Mo_2C/C nanosheets showed excellent catalytic performances due to their embedded structures, highly active surface, and low dispersion density, endowing a high NH_3 yield rate (11.3 μg h^{-1} mg^{-1}) and FE (7.8%) in 0.5 M Li_2SO_4 aqueous solution (pH = 2) for the NRR under ambient conditions (Fig. 4d and e). Moreover, the contrast test demonstrated that the excessive suppression of the HER was not conducive to the NRR activity, although it can lead to a higher FE, revealing that Mo_2C/C was capable of undergoing the NRR catalytic process under strong HER conditions (Fig. 4f–h).

Table 2 Summary of the representative reports on N_2 electroreduction and NH_3 formation using non-noble metal catalysts

Catalyst	Electrolyte	Temperature	NH_3 yield	FE (%)	Potential	Ref.
MoS_2/CC	0.1 M Na_2SO_4	25 °C	4.94 μg h^{-1} cm^{-2}	1.17	−0.5 V *vs.* RHE	48
Mo nanofilm	0.5 M H_2SO_4	25 °C	1.89 μg h^{-1} cm^{-2}	0.72	0.49 V *vs.* RHE	49
Mo_2N	0.1 M HCl	25 °C	27.73 μg h^{-1} cm^{-2}	4.5	−0.3 V *vs.* RHE	51
Fe_2O_3–CNT	0.5 M $LiClO_4$	Room temperature	0.22 μg h^{-1} cm^{-2}	∼0.035	−0.2 V *vs.* Ag/AgCl	54
Fe/Fe_3O_4	0.1 M phosphate buffer solution	Room temperature	8.3 μg h^{-1} cm^{-2}	8.29	−0.3 V *vs.* RHE	56
o-Fe_2O_3–Ar	0.1 M KOH	25 °C	0.46 μg h^{-1} cm^{-2}	6.04	−0.9 V *vs.* Ag/AgCl	57
α-Fe@Fe_3O_4	1 mM H_2SO_4	Room temperature	0.45 ± 0.04 μg h^{-1} cm^{-2}	11.0 ± 0.6	−0.65 V *vs.* NHE	58
Fe_2O_3/AC	NaOH–KOH	250 °C	506.12 μg h^{-1} cm^{-2}	13.7	1.6 cell voltage	59
VN/CC	0.1 M HCl	25 °C	15.18 μg h^{-1} cm^{-2}	3.58	−0.3 V *vs.* RHE	61
VN nanoparticles	0.05 M H_2SO_4	25 °C	20.20 μg h^{-1} cm^{-2}	6.0	−0.1 V *vs.* RHE	62
$Bi_4V_2O_{11}$/CeO_2	HCl, pH = 1	Room temperature	46.42 μg h^{-1} cm^{-2}	10.16	−0.2 V *vs.* RHE	63
TiO_2/Ti	0.1 M Na_2SO_4	25 °C	5.61 μg h^{-1} cm^{-2}	2.5	−0.7 V *vs.* RHE	64
$Ti_3C_2T_x$ MXene	0.1 M Na_2SO_4	25 °C	4.72 μg h^{-1} cm^{-2}	5.78	−0.1 V *vs.* RHE	65
Nb_2O_5 nanofiber	0.1 M HCl	25 °C	17.44 μg h^{-1} cm^{-2}	9.26	−0.55 V *vs.* RHE	66
CoP HNC	1 M KOH	25 °C	5.39 μg h^{-1} cm^{-2}	7.36	−0.4 V *vs.* RHE	67
$CrO_{0.66}N_{0.56}$	1 mM H_2SO_4	Room temperature	5.45 μg h^{-1} cm^{-2}	6.70	2.0 cell voltage	68
Porous Ni	2-Propanol/H_2SO_4	Room temperature	0.942 μg h^{-1} cm^{-2}	0.89	0.5 mA cm^{-2}	69

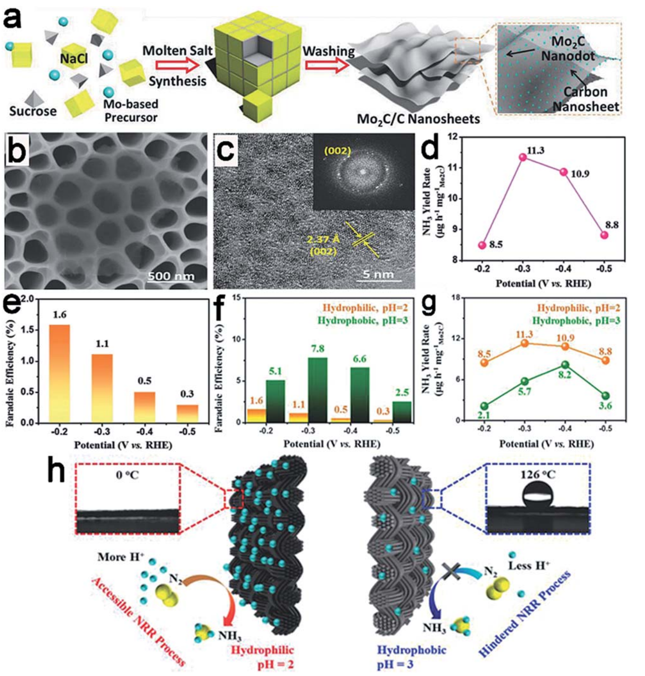

Fig. 4 (a) Illustration of the molten salt synthesis route for Mo_2C/C nanosheets. (b) SEM image and (c) HRTEM image of the Mo_2C/C nanosheets. (d) NH_3 synthesis yield rate and (e) corresponding FE of Mo_2C/C nanosheets. Catalytic performances of Mo_2C/C under proton-suppressed and proton-enriched conditions: (f) NH_3 synthesis FE and (g) corresponding yield rate. (h) NRR catalytic mechanism of Mo_2C/C under proton-suppressed and proton-enriched conditions. Reproduced with permission from ref. 50. Copyright 2018, Wiley-VCH.

In 2014, Licht *et al.* reported a high FE (up to 35%) at 1.2 V, using Fe_2O_3 catalysts in a molten hydroxide electrolyte cell at temperatures ≥200 °C.[53] Unfortunately, the high-temperature electrolysis required a power supply. Recently, Chen *et al.* reported iron supported on carbon nanotubes (Fe_2O_3–CNT) as a catalyst, using water as a hydrogen source and an electrochemical cell with a gas diffusion layer (GDL) electrode as the working electrode (Fig. 5a).[54] The Fe_2O_3–CNT exhibited an NH_3 yield rate of 0.22 μg h^{-1} cm^{-2} under a diluted $KHCO_3$ aqueous solution at room temperature, but only a low FE of 0.15%. Moreover, the possible presence of NH_3 (or NH_4^+) crossover through the Nafion membrane influenced the precise examination. Later, they improved the cell design.[55] The

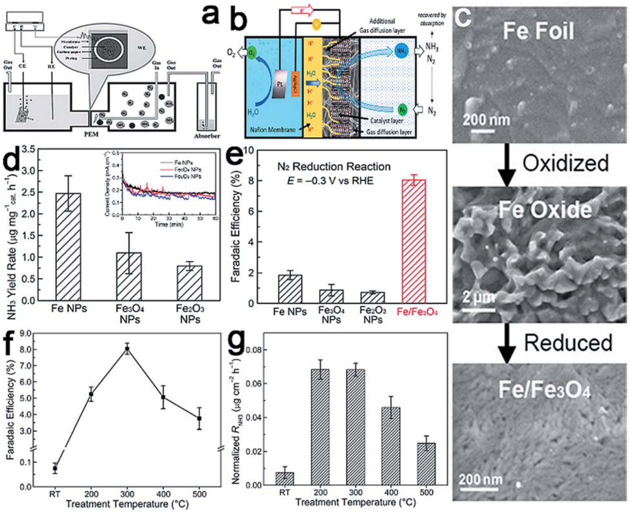

Fig. 5 (a) Schematic view of the electrocatalytic flow reactor for NH_3 synthesis, with the cathode cell operating under electrolyte-less conditions (gas phase). PEM indicates proton exchange membrane. Reproduced with permission from ref. 54. Copyright 2018, Wiley-VCH. (b) Schematic view of the improved design in the three-phase reactor for electrochemical NH_3 synthesis. Reproduced with permission from ref. 55. Copyright 2017, ACS. (c) SEM images of the Fe foil, the 300 °C oxidized sample and the sample after prereduction at −0.5 V *vs.* RHE. (d) NH_3 yield rates of Fe, Fe_3O_4, and Fe_2O_3 nanoparticles measured at −0.3 V *vs.* RHE in N_2-saturated 0.1 M PBS electrolyte. The inset shows THE corresponding chronoamperometric curves. (e) FE of the Fe-based catalysts for NH_3 production at −0.3 V *vs.* RHE. (f) FE of the five samples. (g) Surface-area-normalized NH_3 yield rates of the five samples measured at −0.3 V *vs.* RHE. Reproduced with permission from ref. 56. Copyright 2018, ACS.

concentration of NH_3 in the liquid phase (anode chamber) reached the highest value after 1 h and then decreased, which revealed NH_3 formed in the cathodic part partly passed through the membrane and then reacted in the anode chamber. Some of the NH_3 was consumed, resulting in a decrease in efficiency and NH_3 yield rate. To avoid this negative effect, an additional GDL layer was inserted between the electrocatalyst layer and the Nafion membrane (Fig. 5b), which strongly decreased the NH_3 crossover, and thus the NH_3 collection rate increased. However, it suffered from increased ohmic losses. On the other hand, the Fe_2O_3-based materials were tested under high reduction potentials, which may be possibly reduced to different chemical states such as Fe_3O_4 and Fe. Recently, Feng's group conducted a thorough study on the effect of different chemical states of Fe on the NRR activity.[56] An Fe/Fe_3O_4 catalyst was prepared *via* an oxidization and electrochemical reduction process (Fig. 5c), which exhibited an FE of 8.29% for NH_3 production at −0.3 V *vs.* RHE in phosphate buffer solution. This was superior to that of Fe, Fe_3O_4, and Fe_2O_3 nanoparticles (Fig. 5d and e). Comparative studies of Fe/Fe oxide samples prepared at different oxidation temperatures suggested that the NRR catalytic performance was correlated with the Fe/Fe oxide ratio in the sample (Fig. 5f and g).

Mid-to-late transition-metal-based NRR electrocatalysts such as Fe-, Co-, Ni-, Ru- and Au-based catalysts have been extensively studied, and the early-transition-metal-based electrocatalysts such as V-,[60–63] Ti-[64,65] and Nb-based catalysts[66] are starting to be investigated as well. Yang *et al.* proposed the NRR process on as-synthesized VN nanoparticles *via* a Mars-van Krevelen mechanism.[62] As shown in Fig. 6a, an NH_3 molecule is formed by extracting a surface N atom with adsorbed hydrogen atoms, leaving behind an N vacancy, and the catalyst is regenerated by activating N_2, and thus healing the vacancy. Furthermore, the surface oxygen in the $VN_{0.7}O_{0.45}$ phase is unstable in the reducing environment, leading to faster removal of surface oxygen atoms and generation of surface vacancies. Since the calculated binding energy of N on a vacancy is much higher than that of O, the vacancies are preferentially filled with N, leading to an inactive VN phase. This electrocatalyst achieved a high NH_3 yield rate (20.20 μg h^{-1} cm^{-2}) and FE of (6.0%) at −0.1 V within 1 h. Yu's group constructed an amorphous phase and defective sites within materials to promote their catalytic activity.[63] The fabricated $Bi_4V_2O_{11}/CeO_2$ hybrid with an amorphous phase (BVC-A) (Fig. 6b) was reported to show excellent NRR performances with a high NH_3 yield (46.42 μg h^{-1} cm^{-2} at −0.2 V *vs.* RHE) and high FE (10.16%) (Fig. 6c). CeO_2 not only served as a trigger to induce the amorphous structure, but also established band alignment with $Bi_4V_2O_{11}$ for rapid interfacial charge transfer. The amorphous $Bi_4V_2O_{11}$ contained significant defects, which played a role as active sites. Moreover, the $Bi_4V_2O_{11}/CeO_2$ hybrid with a crystalline phase (BVC-C) showed an inferior performance due to its lack of defects (Fig. 6d). TiO_2 is not a good HER catalyst because of its poor conduction; however, it was reported to be good NRR electrocatalyst by Zhang and co-workwers.[64] The superior NRR activity of their TiO_2 nanosheet array on a Ti plate (TiO_2/Ti) (Fig. 6e) was due to the enhanced adsorption and activation of N_2 by oxygen vacancies *in situ* generated during electrochemical tests. In addition, the nanoarray structure can increase the electrode stability, lower the series resistance, expose more active sites, and facilitate the diffusion of electrolyte and gas. When tested in 0.1 M Na_2SO_4, TiO_2/Ti attained a high NH_3 yield of 5.61 μg h^{-1} cm^{-2} with a corresponding FE of 2.50% at −0.7 V *vs.* RHE. Nb compounds act as promoters or active phases, supports, solid acid catalysts, and redox materials in catalysis. However, Nb_2O_5 was investigated for the first time as an NRR electrocatalyst by Han *et al.*[66] Nb_2O_5 nanofibers (Fig. 6f) were prepared *via* the electrostatic spinning technique, showing a high average NH_3 yield (17.44 μg h^{-1} cm^{-2}) and a high FE (9.26%) at −0.55 V *vs.* RHE (Fig. 6g). DFT calculation indicated the charge exchange and transfer mainly take place between the Nb atoms of the (181) surface and N_2, and the electrons on the adjacent Nb atoms are back transferred to the adsorbed N_2, which activate N_2, and thus result in an extraordinary catalytic performance.

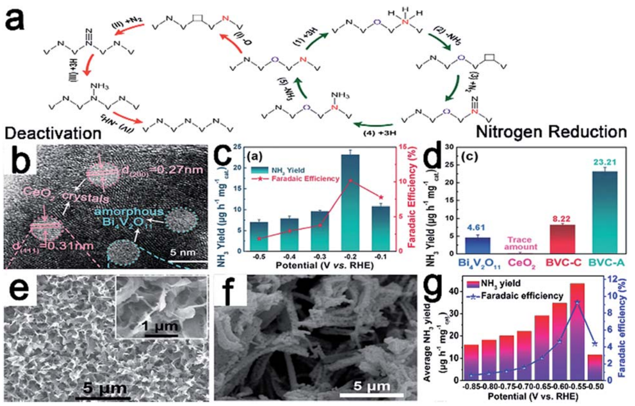

Fig. 6 (a) Proposed reaction pathway for the NRR on the surface of $VN_{0.7}O_{0.45}$ *via* the Mars-van Krevelen mechanism and the catalyst deactivation mechanism. Reproduced with permission from ref. 62. Copyright 2018, ACS. (b) TEM image of BVC-A. (c) Yield of NH_3 (blue-green) and FE (red) at each given potential for BVC-A. (d) Yield of NH_3 with different catalysts at −0.2 V *vs.* RHE. Reproduced with permission from ref. 63. Copyright 2018, Wiley-VCH. (e) SEM images for TiO_2/Ti. Reproduced with permission from ref. 64 copyright 2018, ACS. (f) SEM image of Nb_2O_5 nanofiber. (g) Average NH_3 yields and FEs for Nb_2O_5/CP at a series of potentials. Reproduced with permission from ref. 66. Copyright 2018, Elsevier.

3.3 Metal-free electrocatalysts for the NRR

In the past few years, NRR electrocatalysts have mainly been based on transition-metal-based materials. However, these types of catalysts still have the following limitations:[70,75] (i) most transition metals bind nitrogen too weakly, and are not competent enough for N_2 activation. (ii) The d orbital electrons in transition metals also contribute to the formation of metal–H bonds for the adverse HER, which gives rise to a compromised FE. (iii) Although a few transition metals can handicap the HER at appropriate potentials, feasible alternative mechanisms are urgently needed to achieve reasonable NRR performances. Currently, non-metal inorganic compounds, polymers, and their hybrids have been reported to have great potential as NRR electrocatalysts.

Different from transition metals, which have a combination of unoccupied and occupied d orbitals, main-group compounds generally lack the combination of empty and filled orbitals required to form bonds of s and p symmetry, respectively, and thus very few are able to provide the appropriate energy and symmetry to synergistically accept electron density from and back donate to N_2 (Fig. 7a).[70] Accordingly, the borylene units synthesized by Braunschweig's group acted as a Lewis acid and effectively mimicked transition metals in many reactions. Inspired by this theory, Yu and co-workers developed boron-doped graphene (BG) as an ideal two-dimensional NRR electrocatalyst.[71] The electronegativity of boron (2.04) is smaller than that of carbon (2.55), leading to a clear differentiation of electron densities on the carbon ring structure (Fig. 7b). Thus, the positively charged boron atoms are prone to adsorbing N_2, which offer excellent active centers for the formation of B–N bonds and the subsequent production of NH_3. These electron-deficient boron sites not only furnish strong binding sites for the Lewis base N_2, but also prohibit the binding of the Lewis acid H^+ at these sites (under acidic conditions). As a result, BG demonstrated marvelous NRR activity with the high NH_3 production rate of 9.8 $\mu g\ h^{-1}\ cm^{-2}$ and FE of 10.8% at -0.5 V *vs.* RHE under 0.05 M H_2SO_4 solution (Fig. 7c). Interestingly, boron carbide (B_4C), which possesses high mechanical strength, electrochemical stability, and good electronic conductivity was investigated as a catalyst by Sun's group.[72] In Fig. 7d, the DFT calculation revealed that two main configurations were available for N_2 adsorption on the B_4C (110) surface. In the end-on configuration, only one terminal N atom was bonded to the B atom on the B_4C (110) surface, and in the side-on configuration, two terminal N atoms were separately bonded to two vertical B atoms located on two adjacent boron clusters. This B_4C catalyst exhibited excellent properties both in acid and neutral media.

In terms of the defect engineering strategy, carbon-based materials have been developed as cost-effective electrocatalysts toward the NRR. N-doped porous carbon (NPC) derived from a pyrolyzed zeolite imidazolate framework (Fig. 8a) has attracted great interest in electrochemical reduction reactions.[73] Pyridinic nitrogen and pyrrolic nitrogen have been proposed as the active sites for NH_3 synthesis. Additionally, the porous structure of NPC is beneficial to provide a great number of exposed active sites and fast mass transfer for N_2 adsorption and N≡N cleavage. Nevertheless, the precursor containing CN^- will affect the accurate measurement of the generated NH_3 from N_2. Moreover, there is no evidence to suggest whether the

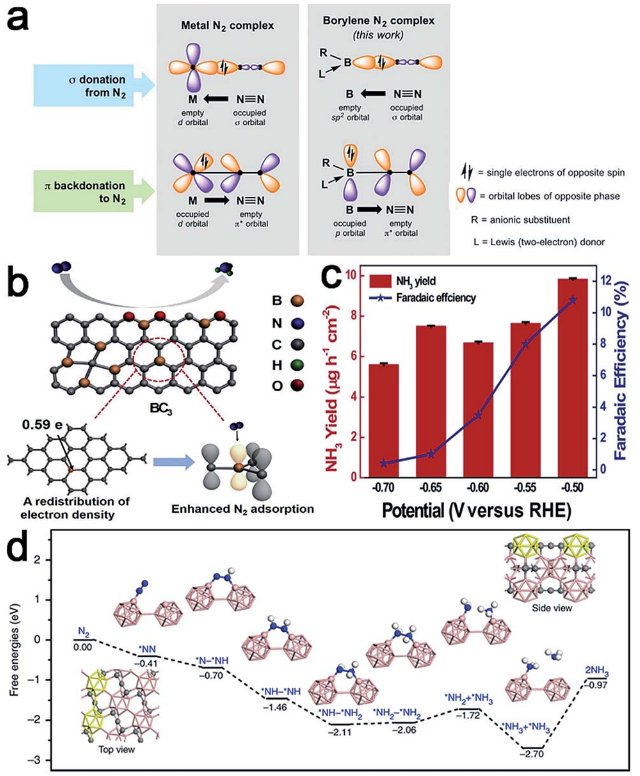

Fig. 7 (a) Simplified schematic of the bonding in well-known end-on-bound transition metal N_2 complexes (left) and prospective application to monovalent boron species (right). Reproduced with permission from ref. 70. Copyright 2018, Science. (b) Schematic of the atomic orbital of BC_3 for binding N_2. (c) NH_3 production rates (left *y* axis) and FE (right *y* axis) of BG. Reproduced with permission from ref. 71 copyright 2018, Elsevier. (d) Density functional theory calculations for B_4C. Color code: blue, N; rose, B; gray, C; white, H; and the asterisk * denotes an adsorption site. Reproduced with permission from ref. 72. Copyright 2018, Nature.

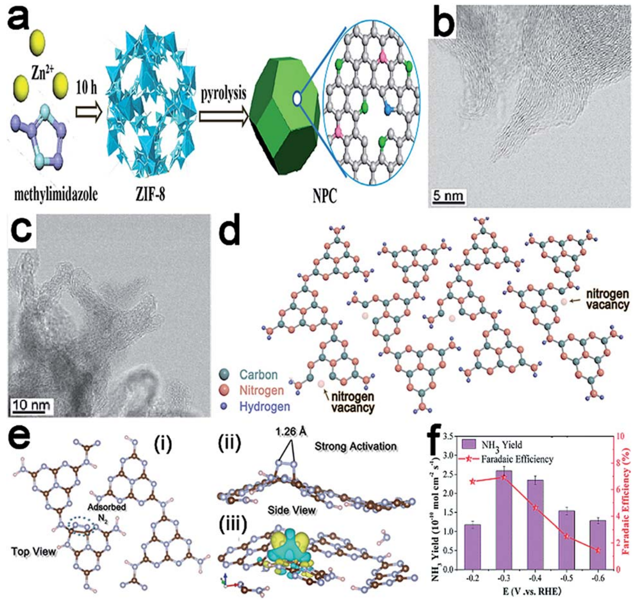

Fig. 8 (a) Schematic of the preparation of NPC. Reproduced with permission from ref. 73. Copyright 2018, ACS. (b) Pristine nanospikes exhibit layers of folded graphene with some structural disorder due to the incorporation of N_2 in their basal plane. (c) Etched nanospikes retain the layered graphene structure but exhibit a much larger radius at the tip, thereby lowering the local electric field present at the tips. Reproduced with permission from ref. 74. Copyright 2018, Science. (d) Schematic of NV engineered polymeric carbon nitride. (e) (i) N_2 adsorption geometry on PCN–NV. (i and iii) Charge density difference of the N_2-adsorbed PCN–NV, where, the yellow and blue isosurfaces represent charge accumulation and depletion in the space, respectively. Reproduced with permission from ref. 75. Copyright 2018, Wiley-VCH. (f) CC at different applied potentials in 0.1 M Na_2SO_4 + 0.02 M H_2SO_4 electrolyte. Reproduced with permission from ref. 76. Copyright 2018, RSC.

nitrogen atoms in the NPC participate in the NRR or not. Intriguingly, Song *et al.* also reported an N-doped carbon material for electrochemically reducing dissolved N_2 gas to NH_3 in an aqueous electrolyte under ambient conditions.[74] The difference is that the morphology of the catalyst is sharp nanospikes (Fig. 8b), concentrating the electric field at their tips, thereby promoting the electroreduction of dissolved N_2 molecules near the electrode. An identical experiment was also conducted with an electrode containing the same amount of nitrogen dopants but the sharp tip texture was fully etched away (Fig. 8c). Since the strong electric field could not be generated, the contrast electrode exhibited poor NRR property. In the same year, Yu's group reported a metal-free polymeric carbon nitride catalyst with nitrogen vacancies (PCN–NV) (Fig. 8d) based on the defect engineering strategy.[75] Their theoretical calculation result demonstrated that N_2 adsorbs on PCN in the dinuclear end-on coordination mode (Fig. 8e(i)) and electrons on the adjacent carbon atoms are transferred to the adsorbed N_2 (Fig. 8e(iii)), which renders the N≡N triple bond intensively weakened with an increased bond length (Fig. 8e(ii)). Notably, Li *et al.* reported that nitrogen-free commercial carbon cloth (CC) was treated by a simple thermal method in air to create rich defects.[76] This nitrogen-free catalyst exhibited superior electrocatalytic activity for the NRR with an NH_3 yield of 15.85 μg h^{-1} cm^{-2} and a FE of 6.92% at 0.3 V *vs.* RHE in a 0.1 M Na_2SO_4 + 0.02 M H_2SO_4 mixture (Fig. 8f). Thus, electrocatalysts prepared using carbon cloth as a substrate and treated under high temperatures may not ignore the contribution of the carbon substrate.[48]

4. NRR electrocatalysis under different electrolyte conditions

Electrolytes are considered a major part of electrochemical N_2 fixation systems. An electrolyte with a limited proton transfer rate and increases the solubility of N_2 can efficiently improve the selectivity. Currently, electrolytes can be divided into four types: liquid electrolytes, polymer electrolytes, solid oxide electrolytes and molten salt electrolytes. Different types of electrolytes can affect the NRR performance and selectivity; hence, it is necessary to choose an optimized electrolyte for a specific electrolytic NRR cell.

4.1 Liquid electrolytes

At present, NRR in liquid electrolyte is one of the most practical reaction under ambient conditions owing to its energy-saving, simple and cost-effective properties. Generally, it is performed in an H-type cell or a single-chamber cell. The chambers are filled with liquid electrolytes such as KOH aqueous solution,[37] HCl aqueous solution,[35] Li-mediated electrolytes,[38,77] organic mixture electrolytes such as, tetrahydrofuran/$LiClO_4$/ethanol solution,[78] methanol/$LiClO_4$/H^+ solution,[79] 2-propanol/deionized water solution[80] and ethylenediamine/LiCl solution,[81] and ionic liquid.[82] Very recently, a novel electrocatalyst system was developed by incorporating Li^+ from the electrolyte into the imide C═O groups on the surface of poly(*N*-ethyl-benzene-1,2,4,5-tetracarboxylic diimide) (PEBCD).[77] Owing to the active O–Li^+ sites in PEBCD, either the Tafel or Heyrovsky reaction path for the HER can be obstructed (Fig. 9a), resulting in a larger potential window to achieve a higher-selectivity NRR. Kim *et al.* studied NH_3 formation in a mixture of water and 2-propanol under ambient conditions in a single chamber (Fig. 9b).[80] More importantly, the existence of 2-propanol in the electrolyte increased the solubility of N_2 and suppressed the competitive HER. Later, they found that 2-propanol was unstable in a reducing environment, which led to an unsatisfactory FE.[81] Thus, the cathodically stable ethylenediamine was introduced as the cathodic electrolyte (Fig. 9c) and a high FE (17.2%) was obtained. Furthermore, a mixture of ionic liquid and trace amount of water as an NRR electrolyte has been investigated. Ionic liquids exhibit considerably high solubility for N_2 and favourable hydrophobic nature, which allows the water content to be controlled at an optimum level to support NH_3 formation, but minimizes the competing HER. As an example of this type of electrolyte, MacFarlane and co-workers reported the use of [C_4mpyr][eFAP] and [$P_{6,6,6,14}$][eFAP] mixed with trace amounts of water as electrolytes and an Fe-based catalyst synthesized *via* the electrodeposition technique as the working electrode for the NRR under ambient conditions.[82] The

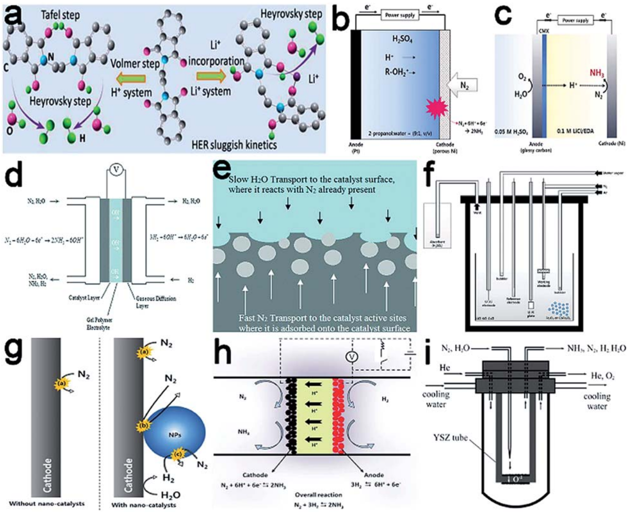

Fig. 9 (a) Schematic of Li^+ association with O sites. Reproduced with permission from ref. 77. Copyright 2017, ACS. (b) Schematic of 2-propanol-based NH_3 formation. Reproduced with permission from ref. 80 copyright 2016, Electrochemical Society, Inc. (c) Schematic of ethylenediamine-based NH_3 synthesis. Reproduced with permission from ref. 81 copyright 2016, Electrochemical Society, Inc. (d) Schematic view of the electrochemical cell based on a polymer gel electrolyte. (e) Schematic of polymer gel electrolyte. Reproduced with permission from ref. 84. Copyright 2018, RSC. (f) Schematic of experimental apparatus for NH_3 synthesis in molten LiCl–KCl–CsCl electrolyte. (g) Scheme of ammonia synthesis mechanism based on the reaction sites on the working electrodes without and with nano-catalysts. Reproduced with permission from ref. 85 copyright 2016, Springer. (h) Schematic of solid oxide cells for electrocatalytic N_2 reduction employing proton-conducting electrolytes. Reproduced with permission from ref. 86. Copyright 2017, Elsevier. (i) Setup of NH_3 synthesis from steam and N_2. Reproduced with permission from ref. 88. Copyright 2009, Elsevier.

test result showed the FE in $[P_{6,6,6,14}]$[eFAP] (60%) is higher than that in $[C_4$mpyr][eFAP] (30%). In addition, DFT calculations indicated that the particular ionic structure of $[P_{6,6,6,14}]$[eFAP] allows N_2 accumulation at the cathode to increase the NRR performance and the additional delocalization of charge onto the three C_2F_5 groups can modulate the charge on the P-bound fluorine atoms to enhance their interaction with N_2 in $[C_4$mpyr][eFAP], leading to high N_2 solubility.

4.2 Polymer electrolytes

Xu *et al.* reported the use of $SmFe_{0.7}Cu_{0.3-x}Ni_xO_3$ as the cathode, NiO–$Ce_{0.8}Sm_{0.2}O_{2-\delta}$ as the anode, and a Nafion membrane as the electrolyte for the synthesis of NH_3 from wet H_2 and dry N_2 at temperatures ranging from 25 °C to 100 °C in a single cell.[83] Compared to high temperature proton conducting materials as electrolytes, the Nafion membrane as the electrolyte achieved a higher current efficiency. However, as the temperature increased, the retention of water molecules decreased, blocking the proton conductivity of the Nafion membrane and resulting in a reduced NRR production rate. Later, Tao and co-workers employed an $H^+/Li^+/NH_4^+$ mixed conducting Nafion membrane as the electrolyte to form NH_3.[44] The mixed NH_4^+/H^+ conducting Nafion membrane increased the chemical compatibility of the acidic Nafion membrane with NH_3. Li^+ ions are capable of reducing the NH_3 formation due to the blocking effect of Li^+ on the transferred protons, rendering a relatively lower current at a higher applied voltage. Moreover, increasing the reaction temperature to 80 °C led to the highest NH_3 formation rate and FE. Recently, Botte's group proposed a novel polymer gel approach to synthesize NH_3 at a low temperature and pressure.[84] This polymer gel electrolyte helped to control the rate of the HER by limiting water transport in the cell; thus, improving the selectivity towards the NRR (Fig. 9d and e). NH_3, a weak base, can react with acid membranes. In their study, an alkaline electrolyte was chosen to enhance the ionic conductivity.

4.3 Molten salt electrolytes

Molten salt electrolytes have been intensively researched due to their high ionic conductivity and relatively mild reaction conditions, thermodynamic stability, wide electrochemical window and low vapor pressure. High-surface area nano-Fe_2O_3 provided iron as a reactive surface to endow high rates of NH_3 generation from air and water under a conducive molten hydroxide (NaOH–KOH) electrolyte at 200 °C.[53] Compared to the melting points of pure alkali hydroxides, eutectic electrolyte have significantly lower melting points. Thus, the NaOH–KOH electrolyte can effectively realize water electrolysis to form H_2 at lower temperatures. In addition, the molten salt of alkali-metal chloride as an electrolyte has been investigated as well. Han's group evaluated the NRR activity of nano-Fe_2O_3 and $CoFe_2O_4$ suspended in a molten LiCl–KCl–CsCl electrolyte at 327 °C (Fig. 9f).[85] Fig. 9g shows schematic cross-sections of the reaction sites on the working electrode with and without the nano-catalysts. For the Ni electrode without the nano-catalysts, there was only one available type of active sites on the Ni surface. After suspending the nano-catalysts in molten chloride, two additional active sites for the catalytic reactions were realized, namely, one at the nanoparticle surface and the other at the electrode/nanoparticle junction. Accordingly, high catalytic activity and electrical conductivity were achieved with the use of the nano-catalyst.

4.4 Solid oxide electrolytes

The working principle of solid oxide systems for N_2 reduction is that the anode and cathode electrodes are deposited on both sides of the proton conductor and H_2 is flowed over the anode to be converted into H^+; then, protons are transported to the cathode, where the half-cell reaction of N_2 and H^+ takes place (Fig. 9h).[86] Iwahara *et al.* reported that $SrCeO_3$ exhibited protonic conductivity in the temperature range of 500–1000 °C.[87] Subsequently, a large number of proton conducting ceramics were synthesized and their conduction properties studied. However, the resulting NH_3 was mixed with feedstock and difficult to separate. In 2009, Skodra and Stoukides modified the electroreduction processes.[88] They used N_2 and steam to synthesize NH_3, which indicates that the further purification of H_2 can be possibly ignored due to the steam. In the electrochemical system, $SrCe_{0.95}Yb_{0.05}O_3$ was employed as the proton conducting solid electrolyte, with Ru-based and Pd catalysts as the cathode and anode, respectively (Fig. 9i). Water vapor was reduced to O_2 and H^+ by electrolysis; then, H^+ was transported to the cathode through a proton conductor disk and reacted with N_2 to synthesize NH_3. More importantly, during the whole reaction process, only N_2 needed to be purified and NH_3 was successfully formed in the temperature range of 450–700 °C. Unfortunately, a low conversion rate of nitrogen or steam into NH_3 was observed due to the poor conductivity of the working electrode and the high reaction temperature increased the energy consumption.

5. Conclusions and prospects

Electrochemical reduction to synthesize NH_3 from N_2 and H_2O directly is considered to be a promising strategy. However, there are still problems and challenges. First, among the researched electrocatalysts for the NRR at ambient conditions, many of them exhibit a low NH_3 yield rate and FE. To date, the superior NH_3 production rates from most reports are dozens of micrograms per hour per square centimeter of catalyst, which is way below the requirement for practical industry applications. Accordingly, significant efforts should be devoted to improving their NRR performance before practical applications. Additionally, the selectivity of most of the current NRR electrocatalysts is still very low, which is dominated by the HER, a major side reaction that shuttles electrons and protons to form H_2, resulting in an FE of less than 10% or even less than 1%. Thus, superior electrocatalysts should be developed to suppress or even circumvent the competing HER to boost selectivity. Tuning crystal facets and defects, controlling atomic doping and d-band centers, and coordinating ligand-introduction and structure vacancies are highly expected to improve the NH_3 yield rate, suppress the HER and enhance the NRR. Moreover, choosing an electrolyte with a limited proton transfer rate and that can increase the solubility of N_2 is another efficient way to improve the selectivity. Second, a standard protocol for electrochemical NRR measurements has not been achieved yet. To date, several types of methods for ammonia detection have been developed, but these approaches are unable to accomplish precise, accurate, repeatable and stable ammonia determination both in low and high concentrations. Therefore, it is highly desired to develop instruments to achieve nanomolar-concentration, continuous monitoring and rapid on-site detection. Third, the process of electroreduction of N_2 to NH_3 is still underexplored. Advanced characterization techniques and electrochemical theory of NRR are highly desired to be developed, such as *in situ* X-ray photoelectron spectroscopy, *in situ* transmission electron microscopy, and *in situ* synchrotron radiation techniques. Fourth, whether NH_3 is synthesized from the N_2 applied in the system is still unclear. This is because the active sites can be poisoned or deactivated after long-time electrochemical tests, and nitrides (present in some catalysts) can decompose under certain potentials. Thus, isotopic $^{15}N_2$ experiments should be performed to further confirm if NH_3 is synthesized from N_2 reduction, particularly for nitrogen-containing catalysts and nitrogen-containing raw materials. Furthermore, most electrochemical measurements are conducted in aqueous media, but the feedstock, N_2, exhibits low solubility in aqueous solution, which lowers the frequency of contact between N_2 and the catalyst surface. Moreover, theoretical calculations have demonstrated that if the access of protons on an electrocatalyst surface can be significantly limited, the adsorption rate of N_2 can surpass that of H^+. Accordingly, gas diffusion devices, low-level proton electrolyte and hydrophobic layer-modified catalyst will hinder proton transfer. Moreover, controlling the surface structure of catalysts is a feasible approach. For example, introducing intrinsic pore structures on the surface of catalysts will provide interfacial cavities for N_2 accumulation.

In summary, the NRR to form NH_3 has strong potential for producing fertilizer, while drastically reducing global energy costs and carbon emissions. Despite the grand challenges ahead, experimental and theoretical calculations can be combined to develop and design more active, selective, efficient, and stable electrocatalysts for NH_3 formation in the near future.

Conflicts of interest

There are no conflicts to declare.

Acknowledgements

This study was financially supported by the National Natural Science Foundation of China (No. 21775089, No. 51572139), the Outstanding Youth Foundation of Shandong Province (No. ZR2017JL010), the Key Research and Development Program of Jining City (2018ZDGH032), and the National Key Research and Development Program of China (No. 2016YFA0203101).

References

1 W. Crabtree, M. S. Dresselhaus and M. V. Buchanan, *Phys. Today*, 2004, **57**, 39–44.

2 D. G. Nocera, *Acc. Chem. Res.*, 2012, **45**, 767–776.

3 P. Yu, L. Wang, Y. Xie, C. Tian, F. Sun, J. Ma, M. Tong, W. Zhou, J. Li and H. Fu, *Small*, 2018, **14**, 1801717.

4 H. Du, X. Zhang, Q. Tan, R. Kong and F. Qu, *Chem. Commun.*, 2017, **53**, 12012–12015.

5 J. Mahmood, F. Li, S.-M. Jung, M. S. Okyay, I. Ahmad, S.-J. Kim, N. Park, H. Y. Jeong and J.-B. Baek, *Nat. Nanotechnol.*, 2017, **12**, 441–446.

6 X. Guo, R. Kong, X. Zhang, H. Du and F. Qu, *ACS Catal.*, 2018, **8**, 651–655.

7 G. Zhang, G. Wang, H. Liu, J. Qu and J. Li, *Nano Energy*, 2018, **43**, 359–367.

8 B. Y. Guan, L. Yu and X. W. Lou, *Angew. Chem., Int. Ed.*, 2017, **56**, 2386–2389.

9 M. Sun, D. Davenport, H. Liu, J. Qu, M. Elimelech and J. Li, *J. Mater. Chem. A*, 2018, **6**, 2527–2539.

10 A. Zitolo, N. Ranjbar-Sahraie, T. Mineva, J. Li, Q. Jia, S. Stamatin, G. F. Harrington, S. M. Lyth, P. Krtil, S. Mukerjee, E. Fonda and F. Jaouen, *Nat. Commun.*, 2017, **8**, 957.

11 R. Chen, J. Yan, Y. Liu and J. Li, *J. Phys. Chem. C*, 2015, **119**, 8032–8037; C. Wu, Y. Zhang, D. Dong, H. Xie and J. Li, *Nanoscale*, 2017, **9**, 12432–12440.

12 H. Mistry, A. S. Varela, C. S. Bonifacio, I. Zegkinoglou, I. Sinev, Y. Choi, K. Kisslinger, E. A. Stach, J. C. Yang, P. Strasser and B. R. Cuenya, *Nat. Commun.*, 2016, **7**, 12123.

13 H. S. Jeon, I. Sinev, F. Scholten, N. J. Divins, I. Zegkinoglou, L. Pielsticker and B. R. Cuenya, *J. Am. Chem. Soc.*, 2018, **140**, 9383–9386.

14 S. Liu, H. Tao, L. Zeng, Q. Liu, Z. Xu, Q. Liu and J. Luo, *J. Am. Chem. Soc.*, 2017, **139**, 2160–2163.

15 I. A. Amar, R. Lan, C. T. G. Petit and S. Tao, *J. Solid State Electrochem.*, 2011, **15**, 1845–1860.

16 S. Giddey, S. P. S. Badwal and A. Kulkarni, *Int. J. Hydrogen Energy*, 2013, **38**, 14576–14594.

17 H. Wang, L. Wang, Q. Wang, S. Ye, W. Sun, Y. Shao, Z. Jiang, Q. Qiao, Y. Zhu, P. Song, D. Li, L. He, X. Zhang, J. Yuan, T. Wu and G. A. Ozin, *Angew. Chem., Int. Ed.*, 2018, **57**, 12360–12364.

18 H. Du, X. Guo, R. Kong and F. Qu, *Chem. Commun.*, 2018, **54**, 12848–12851.

19 X. Ren, J. Zhao, Q. Wei, Y. Ma, H. Guo, Q. Liu, Y. Wang, G. Cui, A. M. Asiri, B. Li, B. Tang and X. Sun, *ACS Cent. Sci.*, 2019, **5**(1), 116–121.

20 G.-F. Chen, S. Ren, L. Zhang, H. Cheng, Y. Luo, K. Zhu, L.-X. Ding and H. Wang, *Small Methods*, 2018, 1800337.

21 S. Mukherjeea, D. A. Cullenb, S. Karakalosc, K. Liud, H. Zhang, S. Zhao, H. Xu, K. L. More, G. Wang and G. Wu, *Nano Energy*, 2018, **48**, 217–226.

22 P. J. Chirik, *Nat. Chem.*, 2009, **1**, 520–522.

23 A. Banerjee, B. D. Yuhas, E. A. Margulies, Y. Zhang, Y. Shim, M. R. Wasielewski and M. G. Kanatzidis, *J. Am. Chem. Soc.*, 2015, **137**, 2030–2034.

24 H. Li, J. Shang, Z. Ai and L. Zhang, *J. Am. Chem. Soc.*, 2015, **137**, 6393–6399.

25 H. Wang, Y. Li, C. Li, K. Deng, Z. Wang, X. Li, H. Xue and L. Wang, *J. Mater. Chem. A*, 2019, **7**, 801–805.

26 J. Zhao, L. Zhang, X. Xie, X. Li, Y. Ma, Q. Liu, W. Fang, X. Shi, G. Cui and X. Sun, *J. Mater. Chem. A*, 2018, **6**, 24031–24035.

27 C. Wu, D. Liu, H. Li and J. Li, *Small*, 2018, **14**, 1704227.

28 X. Zhang, S. Zhu, L. Xia, C. Si, F. Qu and F. Qu, *Chem. Commun.*, 2018, **54**, 1201–1204.

29 S. L. Foster, S. I. P. Bakovic, R. D. Duda, S. Maheshwari, R. D. Milton, S. D. Minteer , M. J. Janik, J. N. Renner and L. F. Greenle, *Nat. Catal.*, 2018, **1**, 490–500.

30 C. J. M. V. D. Ham, M. T. M. Koper and D. G. H. Hetterscheid, *Chem. Soc. Rev.*, 2014, **43**, 5183–5191.

31 N. Bauer, *J. Phys. Chem.*, 1960, **64**, 833–837.

32 A. E. Shilov, *Russ. Chem. Bull.*, 2003, **52**, 2555–2562.

33 M. A. Shipman and M. D. Symes, *Catal. Today*, 2016, **286**, 57–68.

34 E. Skúlason, T. Bligaard, S. Gudmundsdottir, F. Studt, J. Rossmeisl, F. Abild-Pedersen, T. Vegge, H. Jonsson and J. K. Nørskov, *Phys. Chem. Chem. Phys.*, 2012, **14**, 1235–1245.

35 M. Shi, D. Bao, B. Wulan, Y. Li, Y. Zhang, J. Yan and Q. Jiang, *Adv. Mater.*, 2017, **29**, 1606550.

36 S. Li, D. Bao, M. Shi, B. Wulan, J. Yan and Q. Jiang, *Adv. Mater.*, 2017, **29**, 1700001.

37 D. Bao, Q. Zhang, F. Meng, H. Zhong, M. Shi, Y. Zhang, J. Yan, Q. Jiang and X. Zhang, *Adv. Mater.*, 2017, **29**, 1604799.

38 M. Nazemi, S. R. Panikkanvalappila and M. A. El-Sayed, *Nano Energy*, 2018, **49**, 316–323.

39 Z. Wang, Y. Li, H. Yu, Y. Xu, H. Xue, X. Li, H. Wang and L. Wang, *ChemSusChem*, 2018, **11**, 3480–3485.

40 S. Dahl, E. Törnqvist and I. Chorkendorff, *J. Catal.*, 2000, **192**, 381–390.

41 V. Kordali, G. Kyriacou and C. Lambrou, *Chem. Commun.*, 2000, **17**, 1673–1674.

42 R. Manjunatha and A. Schechter, *Electrochem. Commun.*, 2018, **90**, 96–100.

43 R. Lan, J. T. S. Irvine and S. Tao, *Sci. Rep.*, 2013, **3**, 1145.

44 R. Lan and S. Tao, *RSC Adv.*, 2013, **3**, 18016–18021.

45 H. Liu, S. Han, Y. Zhao, Y. Zhu, X. Tian, J. Zeng, J. Jiang, B. Y. Xia and Y. Chen, *J. Mater. Chem. A*, 2018, **6**, 3211–3217.

46 B. K. Burgess and D. J. Lowe, *Chem. Rev.*, 1996, **96**, 2983–3012.

47 R. R. Eady, *Chem. Rev.*, 1996, **96**, 3013–3030.

48 L. Zhang, X. Ji, X. Ren, Y. Ma, X. Shi, Z. Tian, A. M. Asiri, L. Chen, B. Tang and X. Sun, *Adv. Mater.*, 2018, **30**, 1800191.

49 D. Yang, T. Chen and Z. Wang, *J. Mater. Chem. A*, 2017, **5**, 18967–18971.

50 H. Cheng, L. Ding, G. Chen, L. Zhang, J. Xue and H. Wang, *Adv. Mater.*, 2018, **30**, 1803694.

51 X. Ren, G. Cui, L. Chen, F. Xie, Q. Wei, Z. Tian and X. Sun, *Chem. Commun.*, 2018, **54**, 8474–8477.

52 R. Michalsky, Y. J. Zhang, A. J. Medford and A. A. Peterson, *J. Phys. Chem. C*, 2014, **118**, 13026–13034.

53 S. Licht, B. Cui, B. Wang, F. Li, J. Lau and S. Liu, *Science*, 2018, **345**, 637–640.

54 S. Chen, S. Perathoner, C. Ampelli, C. Mebrahtu, D. Su and G. Centi, *Angew. Chem., Int. Ed.*, 2017, **56**, 2699–2703.

55 S. Chen, S. Perathoner, C. Ampelli, C. Mebrahtu, D. Su and G. Centi, *ACS Sustainable Chem. Eng.*, 2017, **5**, 7393–7400.

56 L. Hu, A. Khaniya, J. Wang, G. Chen, W. E. Kaden and X. Feng, *ACS Catal.*, 2018, **8**, 9312–9319.

57 X. Cui, C. Tang, X. Liu, C. Wang, W. Ma and Q. Zhang, *Chem.–Eur. J.*, 2018, **24**, 1–9.

58 B. H. R. Suryanto, C. S. M. Kang, D. Wang, C. Xiao, F. Zhou, L. M. Azofra, L. Cavallo, X. Zhang and D. R. MacFarlane, *ACS Energy Lett.*, 2018, **3**, 1219–1224.

59 B. Cui, J. Zhang, S. Liu, X. Liu, W. Xiang, L. Liu, H. Xin, M. J. Leflerc and S. Licht, *Green Chem.*, 2017, **19**, 298–304.

60 R. Zhang, Y. Zhang, X. Ren, G. Cui, A. M. Asiri, B. Zheng and X. Sun, *ACS Sustainable Chem. Eng.*, 2018, **6**, 9545–9549.

61 X. Zhang, R. Kong, H. Du, L. Xia and F. Qu, *Chem. Commun.*, 2018, **54**, 5323–5325.

62 X. Yang, J. Nash, J. Anibal, M. Dunwell, S. Kattel, E. Stavitski, K. Attenkofer, J. G. Chen, Y. Yan and B. Xu, *J. Am. Chem. Soc.*, 2018, **140**, 13387–13391.

63 C. Lv, C. Yan, G. Chen, Y. Ding, J. Sun, Y. Zhou and G. Yu, *Angew. Chem., Int. Ed.*, 2018, **57**, 6073–6076.

64 R. Zhang, X. Ren, X. Shi, F. Xie, B. Zheng, X. Guo and X. Sun, *ACS Appl. Mater. Interfaces*, 2018, **10**, 28251–28255.

65 Y. Luo, G. Chen, L. Ding, X. Chen, L. Ding and H. Wang, *Joule*, 2019, **3**, 1–11.

66 J. Han, Z. Liu, Y. Ma, G. Cui, F. Xie, F. Wang, Y. Wu, S. Gao, Y. Xu and X. Sun, *Nano Energy*, 2018, **52**, 264–270.

67 W. Guo, Z. Liang, J. Zhao, B. Zhu, K. Cai, R. Zou and Q. Xu, *Small Methods*, 2018, **2**, 1800204.

68 Y. Yao, Q. Feng, S. Zhu, J. Li, Y. Yao, Y. Wang, Q. Wang, M. Gu, H. Wang, H. Li, X. Yuan and M. Shao, *Small Methods*, 2018, DOI: 10.1002/smtd.201800324.

69 K. Kim, N. Lee, C. Yoo, J. Kim, H. C. Yoon and J. Han, *J. Electrochem. Soc.*, 2016, **163**, F610–F612.

70 M. Légaré, G. Bélanger-Chabot, R. D. Dewhurst, E. Welz, I. Krummenacher, B. Engels and H. Braunschweig, *Science*, 2018, **359**, 896–900.

71 X. Yu, P. Han, Z. Wei, L. Huang, Z. Gu, S. Peng, J. Ma and G. Zheng, *Joule*, 2018, **2**, 1–13.

72 W. Qiu, X. Xie, J. Qiu, W. Fang, R. Liang, X. Ren, X. Ji, G. Cui, A. M. Asiri, G. Cui, B. Tang and X. Sun, *Nat. Commun.*, 2018, **9**, 3485.

73 Y. Liu, Y. Su, X. Quan, X. Fan, S. Chen, H. Yu, H. Zhao, Y. Zhang and J. Zhao, *ACS Catal.*, 2018, **8**, 1186–1191.

74 Y. Song, D. Johnson, R. Peng, D. K. Hensley, P. V. Bonnesen, L. Liang, J. Huang, F. Yang, F. Zhang, R. Qiao, A. P. Baddorf, T. J. Tschaplinski, N. L. Engle, M. C. Hatzell, Z. Wu, D. A. Cullen, H. M. Meyer, B. G. Sumpter and A. J. Rondinone, *Sci. Adv.*, 2018, **4**, e1700336.

75 C. Lv, Y. Qian, C. Yan, Y. Ding, Y. Liu, G. Chen and G. Yu, *Angew. Chem., Int. Ed.*, 2018, **57**, 10246–10250.

76 W. Li, T. Wu, S. Zhang, Y. Liu, C. Zhao, G. Liu, G. Wang, H. Zhang and H. Zhao, *Chem. Commun.*, 2018, **54**, 11188–11191.

77 G. Chen, X. Cao, S. Wu, X. Zeng, L. Ding, M. Zhu and H. Wang, *J. Am. Chem. Soc.*, 2017, **139**, 9771–9774.

78 A. Tsuneto, A. Kudo and T. Sakata, *J. Electroanal. Chem.*, 1994, **367**, 183–188.

79 F. Köleli and T. Röpke, *Appl. Catal., B*, 2006, **62**, 306–310.

80 K. Kim, N. Lee, C. Y. Yoo, J. N. Kim, H. C. Yoon and J. I. Han, *J. Electrochem. Soc.*, 2016, **163**, F610–F612.

81 K. Kim, C. Y. Yoo, J. N. Kim, H. C. Yoon and J. I. Han, *J. Electrochem. Soc.*, 2016, **163**, F1523–F1526.

82 F. Zhou, L. M. Azofra, M. Ali, M. Kar, A. N. Simonov, C. McDonnell-Worth, C. Sun, X. Zhang and D. R. MacFarlane, *Energy Environ. Sci.*, 2017, **10**, 2516–2520.

83 G. Xu, R. Liu and J. Wang, *Sci. China, Ser. B: Chem.*, 2009, **52**, 1171–1175.

84 B. L. Sheets and G. G. Botte, *Chem. Commun.*, 2018, **54**, 4250–4253.

85 K. Kim, C. Yoo, J. Kim, H. C. Yoon and J. Han, *Korean J. Chem. Eng.*, 2016, **33**, 1777–1780.

86 X. Guo, Y. Zhu and T. Ma, *J. Energy Chem.*, 2017, **26**, 1107–1116.

87 H. Iwahara, T. Esaka, H. Uchida and N. Maeda, *Solid State Ionics*, 1981, **3**, 359–363.

88 A. Skodra and M. Stoukides, *Solid State Ionics*, 2009, **180**, 1332–1336.